Computer Physics Communications 207 (2016) 287–297

Contents lists available at ScienceDirect

Computer Physics Communications

journal homepage: www.elsevier.com/locate/cpc

A posteriori error control in numerical simulations of semiconductor nanodevices☆

Ren-Chuen Chen [a], Chun-Hsien Li [a], Jinn-Liang Liu [b,*]

[a] Department of Mathematics, National Kaohsiung Normal University, Kaohsiung 802, Taiwan
[b] Department of Applied Mathematics, National Hsinchu University of Education, Hsinchu 300, Taiwan

ARTICLE INFO

Article history:
Received 3 May 2015
Received in revised form
4 January 2016
Accepted 6 July 2016
Available online 17 July 2016

Keywords:
Semiconductors nanodevices
Energy transport
Quantum effect
Boundary and interior layers
A posterior error estimate
Adaptive finite element

ABSTRACT

A posteriori error estimation and control methods are proposed for a quantum corrected energy balance (QCEB) model that describes electron and hole flows in semiconductor nanodevices under the influence of electrical, diffusive, thermal, and quantum effects. The error estimation is based on the maximum norm a posteriori error estimate developed by Kopteva (2008) for singularly perturbed semilinear reaction–diffusion problems. The error estimate results in three error estimators called the first-, second-, and third-order estimators to guide the refinement process. The second-order estimator is shown to be most effective for adaptive mesh refinement. The QCEB model is scaled to a dimensionless coupled system of seven singularly perturbed semilinear PDEs with various perturbation parameters so that the estimator can be applied to each PDE on equal footing. It is found that the estimator suitable for controlling the approximation error of one PDE (one physical variable) may not be suitable for another PDE, indicating that different parameters account for different boundary or interior layer regions as illustrated by two different semiconductor devices, namely, a diode and a MOSFET. A hybrid approach to automatically choosing different PDEs for calculating the estimator in the adaptive mesh refinement process is shown to be able to control the errors of all PDEs uniformly.

1. Introduction

In order to keep pace with the increasing speed of miniaturization of modern semiconductor technology, a great variety of device models that deal with quantum effects, accuracy, robustness, and efficiency in real-life simulations have been intensively developed and tested in recent years, see e.g. [1–17] and references therein. A class of macroscopic quantum mechanical models that are based on the density-gradient (DG) theory of Ancona and Tiersten [1] has been shown to effectively simulate multi-dimensional metal oxide semiconductor field effect transistor devices (MOSFET) [18–20] with gate lengths ranging from 50 nm down to 6 nm [2,4,5,7,8,15,21,22]. The DG theory is derived from Bohm's quantum theory [23] in semiconductor context. It generalizes the equation of state for an ideal electron gas to include DG dependence and corrects the electric field by adding the Bohm potential in the drift term. The macroscopic DG models thus exhibit the essential quantum effects of nonlocality, confinement, and tunneling.

In this paper, we consider in particular the quantum corrected energy balance (QCEB) model proposed in [5] that extends the classical drift–diffusion (DD) model to include the DG quantum potential and energy balance equations in order to deal with both quantum effect and hotspot problems in nanoscale device design [24,25]. The QCEB model has been shown by Jüngel [9] as a simplified balance model that can be derived from the quantum energy transport (QET) equations based on the Chapman–Enskog expansion and Fermi–Dirac distributions. The simplification is made by assuming Maxwellian distributions, parabolic energy band structures, and the inelastic collision approximated by a Fokker–Planck ansatz [9]. For more QET models, we refer to Refs. [9,11,16,21,26].

The QCEB model consists of seven PDEs in which every PDE is self-adjoint and semilinear with respect to its unknown function. The self-adjoint form is due to the Slotboom formulation of continuity and energy balance equations. It is well known that the Slotboom formulation incurs overflow problems in computer implementation for micronscale semiconductor devices to which the applied voltage is much greater than that to nanoscale

☆ This work was supported by NSC under Grant No. 100-2115-M-017-002 to R.C.C. and MOST under Grant No. 103-2115-M-134-004-MY2 to J.L.L., Taiwan.
* Corresponding author.
E-mail address: jinnliu@mail.nhcue.edu.tw (J.-L. Liu).

http://dx.doi.org/10.1016/j.cpc.2016.07.020
0010-4655/

devices. The applied voltage is scaled down to about 1 V in nanodevices. In other words, the overflow problem is no longer a difficult issue for simulating nanodevices by self-adjoint models. Moreover, the ill-conditioning of Slotboom-type matrices in discretization can also be alleviated by suitable scalings for the matrix system [5,27]. The self-adjoint formulation provides many useful properties for the resulting nonlinear algebraic systems such as global convergence and fast linear solvers because Slotboom-type matrices are diagonally dominant M-matrices [28–30] that lead to these appealing properties [5,29–32].

We reformulate the QCEB model here to a dimensionless form of singularly perturbed system involving seven singular perturbation parameters called Debye (one), Planck (two for electrons and holes), DD (two), and EB (two) parameters. The Debye and Planck parameters are conventional parameters related to the electrostatic and quantum effects, respectively. The DD and EB parameters are associated with the diffusivity and thermal conductivity of a device in terms of the electrostatic and quasi-Fermi potentials, respectively. It is shown that the lowest order of the EB parameter is of $O(10^{-33})$ whereas that of the conventional Debye parameter is of $O(10^{-5})$. This indicates that the investigation of singularities in nanodevice models should be extended to all parameters in a model other than just one.

Across the junction between different types of semiconductors in a device or the interface of semiconductors and metal (or oxide), there are thin regions – called interior or boundary layers – of rapid variations of electrostatic and quantum potentials, charge carrier densities, or temperatures [5]. To obtain reliable approximations of layer solutions in an efficient way, one may need to use locally refined meshes that are fine in layer regions and coarse elsewhere. The refinement schemes can be categorized into two classes: *a priori* refinement using special meshes such as those of Shishkin and Bakhvalov [33,34] and *a posteriori* refinement using an adaptive algorithm that automatically generates fine meshes in layer regions starting with a simple initial mesh provided that a reliable error estimator is used to guide the refinement process [35–38]. The first class is very successful for a single PDE for which the layer region is a priori known so that the entire domain can be divided into two uniform-mesh regions, one is coarse and the other is fine. The division is determined by the perturbation parameter [34]. The resulting piecewise-uniform mesh then leads to a uniformly convergent approximation of the singularly perturbed PDE in the discrete maximum norm, i.e., the convergence is independent of the size of the singular perturbation parameter.

The adaptive mesh refinement scheme proposed in this paper belongs to the second class. The first class schemes are not suitable for the QCEB model due to the following reasons. (i) The doping junctions are curves, together with the material interfaces, that may yield overly refined piecewise-uniform meshes. (ii) The QCEB model has seven singular perturbation parameters for which it is impossible to determine a priori their strengths and locations of singularity since these parameters depend on physical conditions that may vary with devices as well as physical conditions.

A variety of a posteriori error estimators have been proposed in the literature. Most of them are based on the global error in weak energy norms for a large class of simple linear elliptic model problems [39–43]. The QCEB model consists of convection–diffusion PDEs in which the transport process dominates in junction and contact regions while the diffusion process is confined to other regions. The current state of error estimators for the convection-dominated problems is still far from satisfactory [44] because the error estimators derived from weak norms depend on an excessive power of the small diffusion parameter [45,46].

The novelty of Kopteva's estimate [33] is that it holds true uniformly in the small diffusion parameter for both boundary and interior layer solutions and is in the maximum norm, which is sufficiently strong to capture the extremely thin layer solutions of nanodevice models. Moreover, it is free of the mesh aspect ratio condition generally required by the standard finite element estimates [33,45]. We find that these properties are quite useful for the 1-irregular rectangular mesh refinement scheme used here, i.e., every finite element edge contains at most one irregular node, since the estimate is derived from finite difference (rectangular) approximation.

Three error estimators, namely, the first-, second-, and third-order estimators can be derived from Kopteva's estimate involving the first, second, and third derivative approximations of the so lution of a singularly perturbed PDE, respectively. It has been shown that the second estimator is most effective for both uniform and Bakhvalov meshes in [33], so as shown in this paper for adaptive mesh. The effectiveness is determined by the ratio of the estimator to the exact error of a constructed PDE in the maximum norm with respect to various degrees of freedom (DOFs) of meshes. The second estimator is then used to guide the refinement process in QCEB simulations on two semiconductor devices, i.e., a diode and a MOSFET. However, a device may exhibit different types of singularities in different regions where different physical properties are governed by different PDEs in a model. For example, the quantum potential of QCEB has a boundary layer near the oxide region while the hot carriers are primarily concentrated along the junction layer or near the drain contact [5]. We thus face a problem of which PDE or which singular perturbation parameter should be used to calculate the estimator during the adaptive refinement process so that the approximation errors of all PDEs in QCEB can be uniformly controlled. The main contribution of the present work is to present a new formulation of QCEB with different types of singular perturbation parameters that can be used to study various layers of state variables in a device and to uniformly control the errors of all these variables. For this, we propose a hybrid method that automatically calculates the estimator via different PDEs in QCEB during the adaptive refinement process.

The rest of the paper is organized as follows. In Section 2, we outline the QCEB model proposed in [5]. A full dimensionless formulation of the model with singular perturbation parameters is then given in Section 3. For clarity, we recall Kopteva's theorem in Section 4 and derive the three error estimators for the 1-irregular mesh refinement scheme. In Section 5, numerical results of a singularly perturbed PDE with exact solution, diode, and MOSFET are given to show the effectiveness of the second estimator, nonuniform convergence of all PDEs with the estimator fixed to one PDE, and uniform convergence with the hybrid error control method. Concluding remarks are given in Section 6.

2. A quantum energy-transport model

The QCEB model of [5] is

$$-\Delta\phi = f_1(\phi) = \frac{q}{\varepsilon}\begin{bmatrix} -n_I \exp\left(\dfrac{\phi+\phi_{qn}}{V_T}\right)\widehat{n} \\ +n_I \exp\left(\dfrac{-\phi-\phi_{qp}}{V_T}\right)\widehat{p} + C \end{bmatrix}, \tag{2.1}$$

$$-\Delta r_n = f_2(r_n) = \frac{-r_n}{2b_n}\left[V_T \ln(r_n^2) - V_T \ln(n_I\widehat{n}) - \phi\right], \tag{2.2}$$

$$-\Delta r_p = f_3(r_p) = \frac{r_p}{2b_p}\left[-V_T \ln(r_p^2) + V_T \ln(n_I\widehat{p}) - \phi\right], \tag{2.3}$$

$$-\nabla\cdot D_4(\phi)\nabla\widehat{n} = f_4(\widehat{n}) = \frac{q\left(n_{eq}p_{eq} - n_I^2\exp(\frac{\phi_{qn}-\phi_{qp}}{V_T})\widehat{n}\widehat{p}\right)}{\tau_0\begin{bmatrix} n_I\exp\left(\dfrac{\phi+\phi_{qn}}{V_T}\right)\widehat{n} + n_I\exp\left(\dfrac{-\phi-\phi_{qp}}{V_T}\right)\widehat{p} \\ +2\sqrt{n_{eq}p_{eq}}\exp\left(\dfrac{\varepsilon_t-\varepsilon_i}{k_BT_L}\right)\end{bmatrix}}, \tag{2.4}$$

$$-\nabla \cdot D_5(\phi)\nabla\widehat{p} = f_5(\widehat{p}) = -f_4(\widehat{n}), \tag{2.5}$$

$$-\nabla \cdot D_6(\varphi_n)\nabla\widehat{T}_n = f_6(\widehat{T}_n) = \mathbf{J}_n \cdot \mathbf{E} + nW_n, \tag{2.6}$$

$$-\nabla \cdot D_7(\varphi_p)\nabla\widehat{T}_p = f_7(\widehat{T}_p) = \mathbf{J}_p \cdot \mathbf{E} + pW_p, \tag{2.7}$$

with the seven unknown functions

$$\begin{cases} \phi,\ r_n = \sqrt{n},\ r_p = \sqrt{p}, \\ \widehat{n} = \dfrac{n}{n_I}\exp\left(\dfrac{-\phi-\phi_{qn}}{V_T}\right),\ \widehat{p} = \dfrac{p}{n_I}\exp\left(\dfrac{\phi+\phi_{qp}}{V_T}\right), \\ \widehat{T}_n = T_n\exp\left(-\dfrac{5\varphi_n}{4V_T}\right),\ \widehat{T}_p = T_p\exp\left(\dfrac{5\varphi_p}{4V_T}\right), \end{cases} \tag{2.8}$$

and the auxiliary relations

$$\phi_{qn} = V_T\ln(r_n^2) - V_T\ln(n_I\widehat{n}) - \phi, \tag{2.9}$$

$$\phi_{qp} = -V_T\ln(r_p^2) + V_T\ln(n_I\widehat{p}) - \phi, \tag{2.10}$$

$$\begin{aligned} D_4(\phi) &= qD_n n_I\exp\left(\frac{\phi+\phi_{qn}}{V_T}\right), \\ D_5(\phi) &= -qD_p n_I\exp\left(\frac{-\phi-\phi_{qp}}{V_T}\right), \end{aligned} \tag{2.11}$$

$$D_6(\varphi_n) = \kappa_n\exp\left(\frac{5\varphi_n}{4V_T}\right),\ D_7(\varphi_p) = \kappa_p\exp\left(\frac{-5\varphi_p}{4V_T}\right), \tag{2.12}$$

$$\mathbf{J}_n = -q\mu_n n\nabla(\phi+\phi_{qn}) + qD_n\nabla n = D_4(\phi)\nabla\widehat{n} = -qn\mathbf{v}_n, \tag{2.13}$$

$$\mathbf{J}_p = -q\mu_p p\nabla(\phi+\phi_{pn}) - qD_n\nabla p = D_5(\phi)\nabla\widehat{p} = qp\mathbf{v}_p, \tag{2.14}$$

$$\omega_{n,p} = \frac{3}{2}k_B T_{n,p} + \frac{1}{2}m^*_{n,p}\left|\mathbf{v}_{n,p}\right|^2,\ \kappa_{n,p} = \frac{2}{q}k_B^2(n,p)\,\mu_{n,p}T_L, \tag{2.15}$$

$$W_n = -\frac{\omega_n-\omega_0}{\tau_{n\omega}},\quad W_p = -\frac{\omega_p-\omega_0}{\tau_{p\omega}}, \tag{2.16}$$

$$\tau_{n,p\omega} = \frac{3\mu_{n,p}k_B T_{n,p}T_L}{2qv_s^2\left(T_{n,p}+T_L\right)} + \frac{m^*_{n,p}\mu_{n,p}T_L}{2qT_{n,p}} \tag{2.17}$$

where ϕ is the electrostatic potential, n and p the electron and hole densities, ϕ_{qn} and ϕ_{qp} the quantum potentials, φ_n and φ_p the generalized quasi-Fermi potentials, $C = -N_A^- + N_D^+$ the doping profile (impurity concentration), $b_n = \frac{\hbar^2}{12m^*_n q}$ and $b_p = \frac{\hbar^2}{12m^*_p q}$ the material parameters measuring the strength of the gradient effects in the electron gas, $\mathbf{E} = -\nabla\phi$ the electric field, $\mathbf{J}_n$ and $\mathbf{J}_p$ the electron and hole current densities, μ_n and μ_p the field-dependent electron and hole mobilities, D_n and D_p the electron and hole diffusion coefficients expressed by the Einstein relation with the mobilities, $\mathbf{v}_n$ and $\mathbf{v}_p$ the electron and hole velocities, ε_i the intrinsic energy, ε_t the trap energy (assuming $\varepsilon_t = \varepsilon_i$), T_n and T_p the electron and hole temperatures, κ_n and κ_p the thermal conductivities, $\tau_{n\omega}$ and $\tau_{p\omega}$ the carrier energy relaxation times, ω_n and ω_p the carrier average energies, v_s the saturation velocity, and other symbols with their values given in Table 2.1.

The system (2.1)–(2.7) models the steady-state of electron and hole flows through a device by adding the quantum potential equations (2.2) and (2.3) to the macroscopic energy transport model (2.1), (2.4)–(2.7). The square roots of carrier densities $r_n = \sqrt{n}$ and $r_p = \sqrt{p}$ in (2.8) were introduced in [4] as extra unknown functions to define the quantum (Bohm) potentials (2.9) and (2.10). These quantum potentials represent first-order quantum corrections of the drift–diffusion fluxes as defined in (2.13) and (2.14). We observe from (2.2) and (2.3) that the QCEB reduces to the classical EB model of in the semiclassical limit $\hbar \to 0$, i.e., $b_{n,p} \to 0$.

Note that the right-hand side nonlinear functionals f_i, $i = 1, \ldots, 7$, in (2.1)–(2.7) are all expressed in terms of their respective unknown variables ϕ, r_n, r_p, $\widehat{n}$, $\widehat{p}$, $\widehat{T}_n$, and $\widehat{T}_p$ to illustrate that each PDE is semilinear with respect to its unknown variable. All functionals are nonlinear due to the Slotboom transformations in (2.8). Furthermore, these transformations imply that all divergence operators on the left-hand side of the system (2.1)–(2.7) are self-adjoint. The Slotboom-type variables $\widehat{T}_n$ and $\widehat{T}_p$ in (2.8) were first introduced in [31]. The Slotboom variables $\widehat{n}$ and $\widehat{p}$ were extended in [5] from the classical Slotboom variables to include the quantum potentials ϕ_{qn} and ϕ_{qp} as shown in (2.8).

Table 2.1
Physical constants.

Symbol	Meaning	Value	Unit
k_B	Boltzmann constant	1.38×10^{-23}	J/K
q	Elementary charge	1.602×10^{-19}	C
m_0	Electron rest mass	9.11×10^{-31}	Kg
m_n^*	Electron effective mass	$0.98 \times m_0$	Kg
m_p^*	Hole effective mass	$0.16 \times m_0$	Kg
ε_0	Permittivity of vacuum	8.85×10^{-14}	F/cm
ε	Silicon dielectric constant	$11.7 \times \varepsilon_0$	F/cm
$\hbar$	Reduced Planck constant	1.054×10^{-34}	J-s
V_T	Thermal voltage	0.0259	V
n_I	Intrinsic carrier concentration	1.5×10^{10}	cm^{-3}
T_L	Lattice temperature	300	K
τ_0	Electron (hole) lifetime	10^{-8}	s
ω_0	Thermal energy	$6.21 \cdot 10^{-21}$	J
μ_n	Electron mobility	1350	cm^2/V-s
μ_p	Hole mobility	480	cm^2/V-s
D_n	Electron diffusion coefficient	34.659	cm^2/s
D_p	Hole diffusion coefficient	12.432	cm^2/s

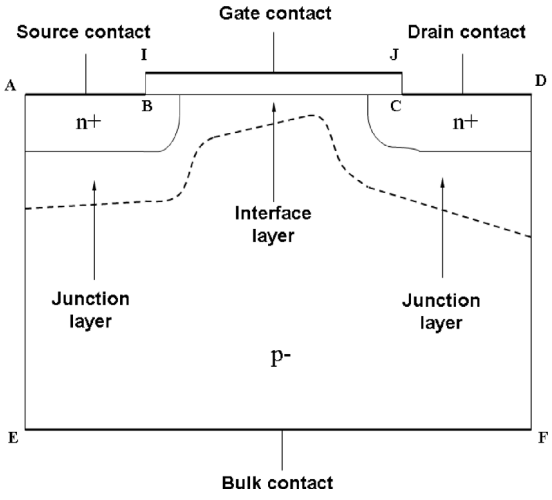

Fig. 1. Geometry of an n-MOSFET device.

Let $\Omega \subset \Re^2$ denote a bounded domain of a doped silicon depicted by Fig. 1. The boundary $\partial\Omega = \partial\Omega_O \cup \partial\Omega_I \cup \partial\Omega_S$ is piecewise smooth with $\partial\Omega_O = \overline{AB} \cup \overline{CD} \cup \overline{EF}$ denoting the Ohmic contacts, $\partial\Omega_I = \overline{BC}$ the silicon/oxide interface, and $\partial\Omega_S = \overline{AE} \cup \overline{DF}$. The boundary conditions for the unknown functions are

$$\begin{cases} \phi = V_O + V_b,\ r_n^2 = \dfrac{1}{2}\left[C + \sqrt{C^2+4n_I^2}\right] \text{ on } \partial\Omega_O, \\ r_p = n_I/r_n \text{ on } \partial\Omega_O,\ r_p = r_n = 0 \text{ on } \partial\Omega_I, \\ \widehat{n} = \exp\left(\dfrac{-V_O}{V_T}\right),\ \widehat{p} = \exp\left(\dfrac{V_O}{V_T}\right) \text{ on } \partial\Omega_O, \\ \widehat{T}_n = \dfrac{300}{\exp\left(\frac{5V_O}{4V_T}\right)},\ \widehat{T}_p = \dfrac{300}{\exp\left(-\frac{5V_O}{4V_T}\right)} \text{ on } \partial\Omega_O, \\ \dfrac{\partial\phi}{\partial\mathbf{n}} = \dfrac{\partial\widehat{n}}{\partial\mathbf{n}} = \dfrac{\partial\widehat{p}}{\partial\mathbf{n}} = \dfrac{\partial r_n}{\partial\mathbf{n}} = \dfrac{\partial r_p}{\partial\mathbf{n}} = \dfrac{\partial\widehat{T}_n}{\partial\mathbf{n}} = \dfrac{\partial\widehat{T}_p}{\partial\mathbf{n}} = 0 \text{ on } \partial\Omega_S, \\ \dfrac{\partial\widehat{n}}{\partial\mathbf{n}} = \dfrac{\partial\widehat{p}}{\partial\mathbf{n}} = \dfrac{\partial\widehat{T}_n}{\partial\mathbf{n}} = \dfrac{\partial\widehat{T}_p}{\partial\mathbf{n}} = 0 \text{ on } \partial\Omega_I, \end{cases} \tag{2.18}$$

where V_O is the applied voltage, V_b is the built-in potential, and $\mathbf{n}$ is an outward normal unit vector to $\partial\Omega_N$. Here the Neumann boundary $\partial\Omega_N$ is a generic notation for which its definition varies with the unknown variables, for example, the Neumann boundary for ϕ and $\widehat{n}$ is $\partial\Omega_N = \partial\Omega_S$ and $\partial\Omega_N = \partial\Omega_S \cup \partial\Omega_I$, respectively. Similarly, the Dirichlet boundary $\partial\Omega_D$ also varies with the variables as manifested in (2.18). The zero Dirichlet boundary conditions for r_p and r_n on the interface $\partial\Omega_I$ are so chosen that the tunneling effect is neglected.

3. A dimensionless QCEB model

Let l be the diameter of a device. By using the following scalings with the new dimensionless quantities marked by the subscript s

$$x_s = \frac{x}{l},\ y_s = \frac{y}{l},\ \nabla_s = \left(\frac{\partial}{\partial x_s}, \frac{\partial}{\partial y_s}\right), \tag{3.1}$$

$$\begin{cases} \phi_s = \dfrac{\phi}{V_T},\ \varphi_{ns} = \dfrac{\varphi_n}{V_T},\ \varphi_{ps} = \dfrac{\varphi_p}{V_T}, \\ \phi_{qns} = \dfrac{\phi_{qn}}{V_T},\ \phi_{qps} = \dfrac{\phi_{qp}}{V_T},\ \mathbf{E}_s = -\nabla_s\phi_s, \\ \varphi_{ms} = \dfrac{\varphi_m}{V_T},\ \varphi_m = \max\limits_{(x,\,y)\in\overline{\Omega}} \left\{|\varphi_n|, |\varphi_p|\right\}, \end{cases} \tag{3.2}$$

$$\begin{cases} C_m = \max\limits_{(x,y)\in\overline{\Omega}} |C(x,y)|, \\ n_s = \dfrac{n}{C_m},\ p_s = \dfrac{p}{C_m},\ r_{ns} = \dfrac{r_n}{\sqrt{C_m}},\ r_{ps} = \dfrac{r_p}{\sqrt{C_m}}, \\ n_{Is} = \dfrac{n_I}{C_m} = \delta,\ C_s = \dfrac{C}{C_m},\ n_{eqs} = \dfrac{n_{eq}}{C_m},\ p_{eqs} = \dfrac{p_{eq}}{C_m}, \\ \widehat{n}_s = \dfrac{\widehat{n}}{\exp(-\varphi_{ms})} = \exp(-\varphi_{ns} + \varphi_{ms}), \\ \widehat{p}_s = \dfrac{\widehat{p}}{\exp(\varphi_{ms})} = \exp(\varphi_{ps} - \varphi_{ms}), \\ n_s = \delta\exp(\phi_s + \phi_{qns} - \varphi_{ms})\widehat{n}_s, \\ p_s = \delta\exp(-\phi_s - \phi_{qns} + \varphi_{ms})\widehat{p}_s \\ \phi_{qns} = \ln(r_{ns}^2) - \ln(\delta\widehat{n}_s) + \varphi_{ms} - \phi_s, \\ \phi_{qps} = -\ln(r_{ps}^2) + \ln(\delta\widehat{p}_s) + \varphi_{ms} - \phi_s, \end{cases} \tag{3.3}$$

$$\begin{cases} \widetilde{D}_4(\phi_s) = \exp(\phi_s + \phi_{qns} - \varphi_{ms}), \\ \widetilde{D}_5(\phi_s) = -\exp(-\phi_s - \phi_{qps} + \varphi_{ms}), \\ \mathbf{J}_{ns} = \dfrac{l\mathbf{J}_n}{qD_n n_I} = \widetilde{D}_4(\phi_s)\nabla_s\widehat{n}_s, \\ \mathbf{J}_{ps} = \dfrac{l\mathbf{J}_p}{qD_p n_I} = \widetilde{D}_5(\phi_s)\nabla_s\widehat{p}_s, \end{cases} \tag{3.4}$$

$$\begin{cases} T_{ns} = \dfrac{T_n}{T_m},\ T_{ps} = \dfrac{T_p}{T_m},\ T_{Ls} = \dfrac{T_L}{T_m},\ T_m = \max\limits_{(x,\,y)\in\overline{\Omega}} \left\{T_n, T_p\right\}, \\ \widehat{T}_{ns} = \dfrac{\widehat{T}_n}{T_m \exp\left(\frac{-5\varphi_{ms}}{4}\right)} = T_{ns}\exp\left(\dfrac{-5}{4}(\varphi_{ns} - \varphi_{ms})\right), \\ \widehat{T}_{ps} = \dfrac{\widehat{T}_p}{T_m \exp\left(\frac{5\varphi_{ms}}{4}\right)} = T_{ps}\exp\left(\dfrac{5}{4}(\varphi_{ps} - \varphi_{ms})\right), \\ \widetilde{D}_6(\varphi_{ns}) = \exp\left(\dfrac{5}{4}(\varphi_{ns} - \varphi_{ms})\right), \\ \widetilde{D}_7(\varphi_{ps}) = \exp\left(\dfrac{-5}{4}(\varphi_{ps} - \varphi_{ms})\right), \\ W_{ns} = \dfrac{l^2 W_n}{qD_n V_T},\ W_{ps} = \dfrac{l^2 W_p}{qD_p V_T},\ \tau_{n\omega s} = \dfrac{\tau_{n\omega}}{k_B T_L},\ \tau_{p\omega s} = \dfrac{\tau_{p\omega}}{k_B T_L}, \end{cases} \tag{3.5}$$

Table 3.1
Singular perturbation parameters.

$\epsilon_1 = \sqrt{\frac{\varepsilon V_T}{l^2 q C_m}}$	Scaled Debye length
$\epsilon_2 = \sqrt{\frac{\hbar^2}{6m_n^* q V_T l^2}}$	Scaled Planck constant
$\epsilon_3 = \sqrt{\frac{\hbar^2}{6m_p^* q V_T l^2}}$	Scaled Planck constant
$\epsilon_4 = \sqrt{\frac{\delta\widetilde{D}_4(\phi)}{\beta_n}}$	Scaled DD parameter
$\epsilon_5 = \sqrt{\frac{-\delta\widetilde{D}_5(\phi)}{\beta_p}}$	Scaled DD parameter
$\epsilon_6 = \sqrt{\frac{\kappa_n T_m \widetilde{D}_6(\varphi_n)}{qD_n V_T C_m}}$	Scaled EB parameter
$\epsilon_7 = \sqrt{\frac{\kappa_p T_m \widetilde{D}_7(\varphi_p)}{qD_p V_T C_m}}$	Scaled EB parameter

the QCEB model (2.1)–(2.7) can be transformed to (after dropping the subscript s for simplicity)

$$-\epsilon_1^2\Delta\phi = f_1(\phi) = \begin{bmatrix} -\delta\exp(\phi + \phi_{qn} - \varphi_m)\widehat{n} + \\ \delta\exp(-\phi - \phi_{qp} + \varphi_m)\widehat{p} + C \end{bmatrix} \tag{3.6}$$

$$-\epsilon_2^2\Delta r_n = f_2(r_n) = -r_n\left[2\ln\left(\delta^{-1/2}r_n\right) + \varphi_n - \phi\right], \tag{3.7}$$

$$-\epsilon_3^2\Delta r_p = f_3(r_p) = r_p\left[-2\ln\left(\delta^{-1/2}r_p\right) + \varphi_p - \phi\right], \tag{3.8}$$

$$-\nabla\cdot(\epsilon_4^2\nabla\widehat{n}) = f_4(\widehat{n}) \tag{3.9}$$

$$= \frac{\left(n_{eq}p_{eq} - \delta^2\exp(\phi_{qn} - \phi_{qp})\widehat{n}\widehat{p}\right)}{\left[\begin{array}{l}\delta\exp(\phi + \phi_{qn} - \varphi_m)\widehat{n} + \\ \delta\exp(-\phi - \phi_{qp} + \varphi_m)\widehat{p} + 2\sqrt{n_{eq}p_{eq}}\exp\left(\dfrac{\varepsilon_t - \varepsilon_i}{k_B T}\right)\end{array}\right]},$$

$$-\nabla\cdot(\epsilon_5^2\nabla\widehat{p}) = -f_5(\widehat{p}) = f_4(\widehat{n}) \tag{3.10}$$

$$-\nabla\cdot\left(\epsilon_6^2\nabla\widehat{T}_n\right) = f_6(\widehat{T}_n) = \delta\mathbf{J}_n\cdot\mathbf{E} + nW_n, \tag{3.11}$$

$$-\nabla\cdot\left(\epsilon_7^2\nabla\widehat{T}_p\right) = f_7(\widehat{T}_p) = \delta\mathbf{J}_p\cdot\mathbf{E} + pW_p, \tag{3.12}$$

where

$$\begin{cases} \epsilon_1^2 = \dfrac{\varepsilon V_T}{l^2 q C_m},\ \epsilon_2^2 = \dfrac{\hbar^2}{6m_n^* q V_T l^2},\ \epsilon_3^2 = \dfrac{\hbar^2}{6m_p^* q V_T l^2}, \\ \epsilon_4^2 = \delta\widetilde{D}_4(\phi)/\beta_n,\ \epsilon_5^2 = -\delta\widetilde{D}_5(\phi)/\beta_p, \\ \beta_n = \dfrac{l^2}{D_n\tau_0},\ \beta_p = \dfrac{l^2}{D_p\tau_0}, \\ \epsilon_6^2 = \kappa_n T_m\widetilde{D}_6(\varphi_n)/(qD_n V_T C_m), \quad \epsilon_7^2 = \kappa_p T_m\widetilde{D}_7(\varphi_p)/(qD_p V_T C_m). \end{cases} \tag{3.13}$$

The seven singular perturbation parameters in the system (3.6)–(3.12) are summarized in Table 3.1, where $\epsilon_{4,5}$ and $\epsilon_{6,7}$ are called the scaled DD and EB parameters for the DD ((3.9), (3.10)) and EB ((3.11), (3.12)) equations, respectively. The singularity of $\epsilon_{4,5}$ and $\epsilon_{6,7}$ is governed by the exponential functionals $\widetilde{D}_{4,5}(\phi)$ and $\widetilde{D}_{6,7}(\varphi_{n,p})$, respectively. These functionals are characterized by the electrostatic ϕ and quasi-Fermi $\varphi_{n,p}$ potentials. The first three parameters $\epsilon_{1,2,3}$ are conventional. For convenience, the main state variables and various symbols of the system are summarized in Table 3.2.

4. Error indicators and estimators

We use the linear finite element (FE) method, together with the Scharfetter–Gummel exponential scheme proposed in [31] for the DD and EB equations, to approximate all PDEs in the QCEB model (3.6)–(3.12) and solve the resulting nonlinear algebraic system of each PDE one by one as in Gummel's iteration method until all tolerable approximate solutions are reached [5]. In weak form,

Table 3.2
Model notation.

ϕ	Electrostatic potential	$\delta = \frac{n_I}{C_m}$
ϕ_{qn}, ϕ_{qp}	Quantum potentials	
n, p	Electron, hole densities	$r_n = \sqrt{n}, r_p = \sqrt{p}$
T_n, T_p	Electron, hole temperatures	
φ_n, φ_p	Quasi-Fermi potentials	$\varphi_m = \max\{\lvert\varphi_n\rvert, \lvert\varphi_p\rvert\}$
C	Doping (impurity) concentration	$C_m = \max C$
κ_n, κ_p	Thermal conductivities	$T_m = \max T$
l	Scaling length	$\beta_n = \frac{l^2}{D_n \tau_0}, \beta_p = \frac{l^2}{D_p \tau_0}$

each semilinear PDE is equivalent to the following strong form for the finite difference method as considered in [33].

The following a posteriori error estimation theorem is proved in [33] for the central finite difference approximation of a 2D singularly perturbed semilinear elliptic PDE with regular meshes on domain discretization.

Theorem 1. *Let $u(x, y)$ be a solution of the semilinear PDE*

$$\begin{cases} -\epsilon^2 \triangle u + b(x, y, u) = 0, \ (x, y) \in \Omega = (0, 1) \times (0, 1), \\ u(x, y) = 0, \ (x, y) \in \partial\Omega, \\ 0 < \beta < \dfrac{\partial b(x, y, u)}{\partial u} \le \overline{\beta}, \ \forall (x, y, u) \in [0, 1]^2 \times R^1, \end{cases} \tag{4.1}$$

where β and $\overline{\beta}$ are constants. Let U_{ij} satisfy the standard five-point finite difference equations

$$-\epsilon^2 D_x^2 U_{ij} - \epsilon^2 D_y^2 U_{ij} + b(x_i, y_j, U_{ij}) = 0, \tag{4.2}$$

for $i = 1, \ldots, N, j = 1, \ldots, M$, where $U_{1,j} = U_{N,j} = U_{i,1} = U_{i,M} = 0$ and N and M are the numbers of grid points in the x- and y-axis, respectively. Let $U^B(x, y)$ be a piecewise bilinear interpolant of U_{ij} on each $[x_{i-1}, x_i] \times [y_{j-1}, y_j]$ in $\overline{\Omega}$ such that $U^B(x_i, y_j) = U_{ij}$. Then the a posteriori error

$$\eta = \max_l \{\eta^{(l)}\}, \ \eta^{(l)} = h^2 M^{(l)}, \ l = 0, 1, 2, 3, \tag{4.3}$$

is bounded from below by the exact error $e = \left\| U^B - u \right\|_\infty$ as

$$e \le \widetilde{C}\eta, \tag{4.4}$$

where

$$\begin{cases} M^{(0)} = 1 \\ M^{(1)} \\ \quad = \max\limits_{i,j} \left\{ \left|D_x^- U_{i,j}\right|^2, \left|D_x^- U_{i,j-1}\right|^2, \left|D_y^- U_{i,j}\right|^2, \left|D_y^- U_{i,j-1}\right|^2 \right\} \\ M^{(2)} \\ \quad = \max\limits_{i,j} \left\{ \begin{matrix} \left|D_x^2 U_{i-1,j}\right|, \left|D_x^2 U_{i,j}\right|, \left|D_x^2 U_{i-1,j-1}\right|, \left|D_x^2 U_{i,j-1}\right|, \\ \left|D_y^2 U_{i,j-1}\right|, \left|D_y^2 U_{i,j}\right|, \left|D_y^2 U_{i-1,j-1}\right|, \left|D_y^2 U_{i-1,j}\right| \end{matrix} \right\} \\ M^{(3)} = \epsilon \max\limits_{i,j} \left\{ \begin{matrix} \left|D_x^- D_x^2 U_{i,j}\right|, \left|D_x^- D_x^2 U_{i,j-1}\right|, \\ \left|D_y^- D_y^2 U_{i,j}\right|, \left|D_y^- D_y^2 U_{i-1,j}\right| \end{matrix} \right\} \end{cases} \tag{4.5}$$

$$\begin{cases} D_x^- U_{i,j} = \dfrac{U_{i,j} - U_{i-1,j}}{h_i}, \ D_x^2 U_{i,j} = \dfrac{D_x^- U_{i+1,j} - D_x^- U_{i,j}}{(h_i + h_{i+1})/2}, \\ D_y^- U_{i,j} = \dfrac{U_{i,j} - U_{i,j-1}}{k_j}, \ D_y^2 U_{i,j} = \dfrac{D_y^- U_{i,j+1} - D_y^- U_{i,j}}{(k_j + k_{j+1})/2}, \end{cases} \tag{4.6}$$

$h = \max_{i,j}\{h_i, k_j\}, h_i = x_i - x_{i-1}, k_j = y_j - y_{j-1}, \widetilde{C} = C_0 \ln(2 + \epsilon/h)$, and the constant C_0 is independent of ϵ and the mesh size h. Here $\eta^{(l)}$ and $M^{(l)}$, $l = 1, 2, 3$, involve discrete analogues of lth-order derivatives.

We extend applications of the theorem to the finite element (FE) approximation with 1-irregular adaptive meshes [29,31] as follows. Let $\mathcal{T}$ be a FE partition of the domain $\overline{\Omega}$ such that $\mathcal{T} = \{\tau_k; \ k = 1, \ldots, L, \ \overline{\Omega} = \bigcup_{k=1}^{L} \overline{\tau}_k\}$ and $S_h(\mathcal{T})$ denotes a FE subspace on $\mathcal{T}$ for the given problem. The FE approximation of the problem in $S_h(\mathcal{T})$ is then to find $u_h \in S_h(\mathcal{T})$ such that

$$B_h(u_h, v_h) = F(v_h) \quad \forall v_h \in S_h(\mathcal{T}), \tag{4.7}$$

with

$$\begin{aligned} B_h(u_h, v_h) &= \epsilon^2 \sum_{\tau \in \mathcal{T}} \int_\tau \nabla u_h \cdot \nabla v_h \, dxdy, \\ F_h(v_h) &= -\sum_{\tau \in \mathcal{T}} \int_\tau b(u_h) v_h \, dxdy. \end{aligned} \tag{4.8}$$

We consider particularly that the partition $\mathcal{T}$ is generated by the 1-irregular mesh refinement scheme such that the resulting finite element space $S_h(\mathcal{T})$ consists of continuous functions by means of constrained bilinear bases [31,47]. A node is called *regular* if it constitutes a vertex for each of the neighboring elements; otherwise it is *irregular*. Without loss of generality, the error indicators

$$\eta_k^{(l)} = h_k^2 M^{(l)}, \ l = 1, 2, 3, \tag{4.9}$$

for each element τ_k can be defined as follows.

Type 0 (without irregular nodes): This is a 12-point stencil grid as shown in Fig. 2, where all nodes are regular. Then, $M^{(l)}$, $l = 1, 2, 3$, are defined as in (4.5).

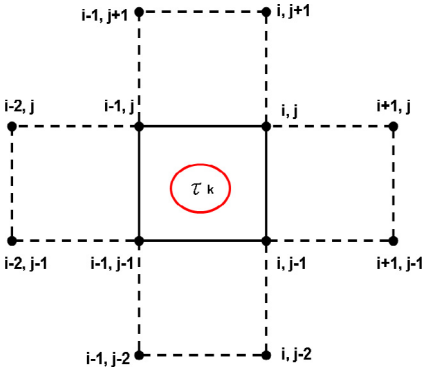

Fig. 2. A regular mesh.

Type 1 (with one irregular node): Fig. 3 illustrates a typical case of this type of elements, where $(i - 1, j)$ marked by the cross sign is the only irregular node in the element. For other cases, the error indicators are defined in a similar way. We can approximate the solution $U_{i-1,j}$ by $\frac{U_{i-1,j+1} + U_{i-1,j-1}}{2}$. Since $U_{i-1,j}$ is a first-order approximation and cannot be used to define the second- and third-order error indicators in the y coordinate, the error indicators $\eta_k^{(l)}$ are hence defined by

$$\begin{cases} M^{(1)} = \max\left\{ \left|D_x^- U_{i,j}\right|^2, \left|D_y^- U_{i,j}\right|^2, \left|D_x^- U_{i,j-1}\right|^2, \left|D_y^- U_{i-1,j}\right|^2 \right\} \\ M^{(2)} = \max\left\{ \begin{matrix} \left|D_x^2 U_{i,j}\right|, \left|D_x^2 U_{i,j-1}\right|, \\ \min\{\left|D_y^2 U_{i,j-1}\right|, \left|D_y^2 U_{i,j}\right|\}, \left|D_y^2 U_{i-1,j-1}\right| \end{matrix} \right\} \\ M^{(3)} = \epsilon \max\left\{ \left|D_y^- D_y^2 U_{i,j}\right| \right\}. \end{cases} \tag{4.10}$$

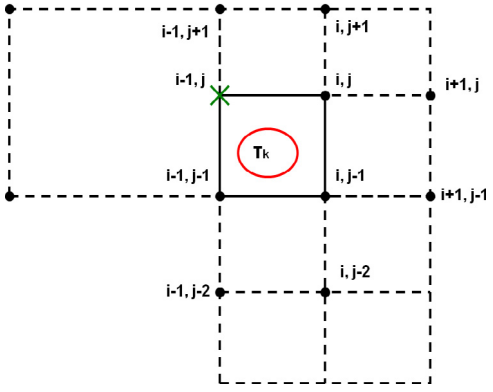

Fig. 3. A 1-irregular mesh with one irregular node marked by the cross sign.

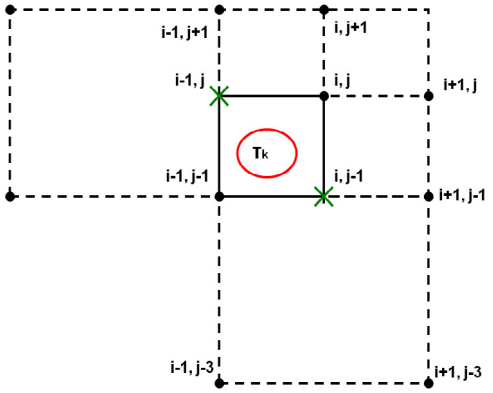

Fig. 4. A 1-irregular mesh with two irregular nodes.

Type 2 (with two irregular nodes): Fig. 4 illustrates a typical case of this type of elements, where $(i-1, j)$ and $(i, j-1)$ are irregular. Let $U_{i-1,j} = \frac{U_{i-1,j+1}+U_{i-1,j-1}}{2}$ and $U_{i,j-1} = \frac{U_{i-1,j-1}+U_{i+1,j-1}}{2}$. The error indicators $\eta_k^{(l)}$ are defined by

$$\begin{cases} M^{(1)} \\ \quad = \max\left\{\left|D_x^- U_{i,j}\right|^2, \left|D_x^- U_{i,j-1}\right|^2, \left|D_y^- U_{i,j}\right|^2, \left|D_y^- U_{i,j-1}\right|^2\right\} \\ M^{(2)} = \max\left\{\left|D_x^2 U_{i,j}\right|, \left|D_y^2 U_{i,j}\right|\right\} \\ M^{(3)} = 0. \end{cases} \tag{4.11}$$

In the 1-irregular mesh refinement process, we need to decide which elements should be divided into four subelements. A permissible error $\eta_\gamma^{(l)}$ for all elements in $\mathcal{T}$ can be defined as

$$\eta_\gamma^{(l)} = \gamma \max_{\tau_k \in \mathcal{T}} \eta_k^{(l)}, \tag{4.12}$$

where the refinement factor $0 < \gamma \leq 1$ is an empirical value for which we choose $\gamma = 0.1$ [48]. If the *error indicator* $\eta_k^{(l)}$ in the element τ_k exceeds $\eta_\gamma^{(l)}$, this element will be divided. To keep the 1-irregularity requirement, some elements will be divided even though their error indicators do not exceed the permissible error, depending on the refinement condition of their neighboring elements [47]. The largest error indicator $\eta^{(l)} = \max_{\tau_k \in \mathcal{T}} \eta_k^{(l)}$ for each $l = 1, 2, 3$ is called an *error estimator*.

5. Numerical results

Three examples are given to investigate error estimators and control. We first determine which of the above three estimators is most effective in adaptive computation by using a singularly perturbed PDE whose exact solution is known. The most effective estimator is then used to control errors in simulating diode and MOSFET by the QCEB model.

Example 1. We consider the reaction dominated problem

$$\begin{cases} -\epsilon^2 \triangle u + u = f(x, y), \ (x, y) \in \Omega = (0, 1) \times (0, 1), \\ u(x, y) = 0, \ (x, y) \in \partial\Omega, \end{cases} \tag{5.1}$$

with the exact solution

$$u(x, y) = (e^{-x/\epsilon} - 1)(x - 1)y(1 - y),$$

where ϵ is a small parameter.

As mentioned in Section 1, the existing error estimators derived in various weak norms fail to produce appropriate meshes for various examples [44] of convection-dominated problems. This is because those estimators depend on an excessive power of the small diffusion parameter ϵ and are thus not effective to estimate exact errors of approximated layer solutions with varying ϵ [45], i.e., those estimators are not uniformly effective in ϵ. On the other hand, the maximum-norm estimator $\eta = \max_l\{\eta^{(l)}\}$ for $l = 1, 2, 3$, has been shown to be uniformly effective in ϵ for the singularly perturbed problem (5.1) in [33].

Using the estimators $\eta^{(l)}$, adaptive meshes and solution contours of this problem are shown in Fig. 5 with various degrees of freedom (DOFs) denoting the total number of regular nodes of a particular mesh. The adaptive meshes are generated from a very coarse mesh by means of (4.12) without using any a priori information about the singular parameter. As expected, the grid is refined in the boundary layer as shown in the figures, i.e., all three estimators correctly capture the boundary layer.

The question is which estimator is most effective for adaptive mesh. Since the exact solution is known, the effectiveness of an estimator $\eta^{(l)}$ is usually quantified by the effectiveness ratio $\eta^{(l)}/e$ with respect to DOFs, where e denotes the maximum error norm $e = \max_{i,j}\left\{\left|U_{i,j} - u(x_i, y_j)\right|\right\}$. The estimator is effective if the ratio $\eta^{(l)}/e$ remains constant with varying DOFs as implied by the a posteriori estimate (4.4) in which the constant $\widetilde{C}$ is independent of the mesh size h (DOFs) and the singular parameter ϵ. We observe from Tables 5.1 and 5.2 that the first-order $\eta^{(1)}$ and third-order $\eta^{(3)}$ estimators are degraded as DOFs increase for both $\epsilon = 10^{-4}$ and 10^{-8} whereas the second-order estimator $\eta^{(2)}$ is quite stable. Note that the estimator $\eta^{(2)}$ was shown to be most effective in [33] as well for either uniform or Bakhvalov mesh. We therefore use $\eta^{(2)}$ to control errors in adaptive QCEB computation for the following two devices.

Example 2. For simplicity, the second-order estimator $\eta^{(2)}$ is denoted by η in this and next example omitting the superscript (2). The error control of adaptive approximation is first investigated by a typical $n^+ - n - n^+$ diode illustrated in Fig. 6, where the bold lines indicate Ohmic contacts. Contacts AB and AF are terminated at a distance of 20 nm from the top left corner without extending to the full n^+ region as in realistic diodes. The channel length L is 38 nm. The doping profiles are 5.0×10^{19} cm^{-3} and 2.0×10^{15} cm^{-3} in the highly and lowly doped region, respectively. The applied voltage is 0.85 V. For n-type semiconductors the electron is referred to as the majority carrier and the hole as the minority carrier since the electron concentration is much larger. Therefore, we do not consider the hole equations (3.8), (3.10) and (3.12) for the diode.

Under these physical conditions, the numerical range of the four singular parameters ϵ_1 (Debye), ϵ_2 (Planck), ϵ_4 (DD), and ϵ_6 (EB) in the four PDEs (3.6), (3.7), (3.9), and (3.11), respectively, is given in Table 5.3. The range varies widely as shown by various orders in the table. We thus need to determine which PDE (or parameter)

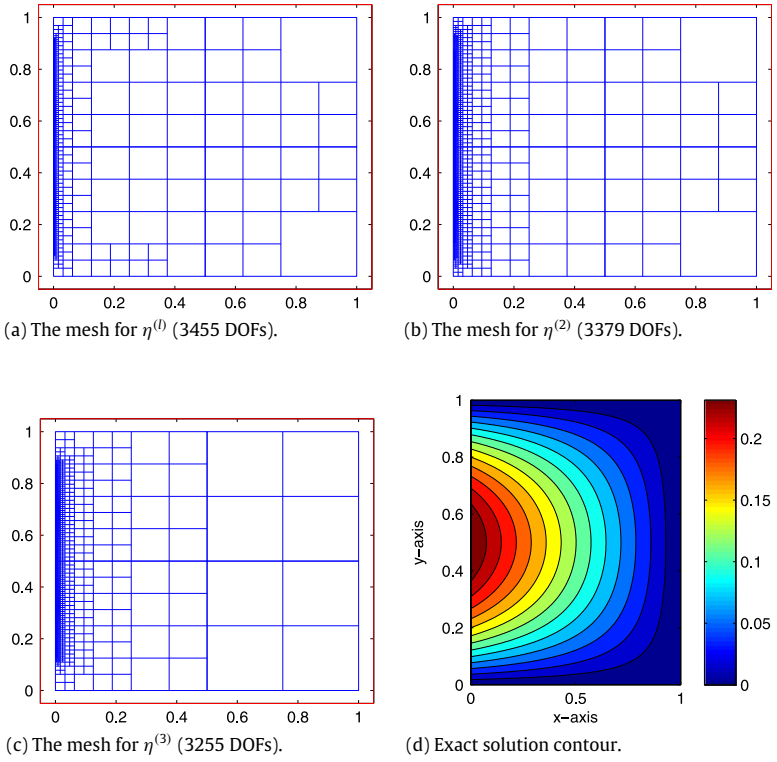

(a) The mesh for $\eta^{(l)}$ (3455 DOFs). (b) The mesh for $\eta^{(2)}$ (3379 DOFs).

(c) The mesh for $\eta^{(3)}$ (3255 DOFs). (d) Exact solution contour.

Fig. 5. Adaptive meshes and solution contour of Example 1 with $\epsilon^2 = 10^{-8}$.

Table 5.1
$\epsilon^2 = 10^{-4}$: Exact error in maximum norm e and effectiveness ratio $\eta^{(l)}/e$.

DOFs	e	$\eta^{(1)}/e$	DOFs	e	$\eta^{(2)}/e$	DOFs	e	$\eta^{(3)}/e$
269	0.01897	0.95	439	0.03572	2.92	508	0.03568	1.64
973	0.00970	0.67	1343	0.01902	3.01	1356	0.01895	2.18
2807	0.00453	0.43	3390	0.00969	3.05	3975	0.00976	2.47
10501	0.00226	0.23	8924	0.00451	3.36	10737	0.00780	1.64
41251	0.00076	0.18	21200	0.00213	3.05	25518	0.00780	0.88
163197	0.00033	0.11	49930	0.00071	3.97	48470	0.00780	0.47

Table 5.2
$\epsilon^2 = 10^{-8}$: Exact error in maximum norm e and effectiveness ratio $\eta^{(l)}/e$.

DOFs	e	$\eta^{(1)}/e$	DOFs	e	$\eta^{(2)}/e$	DOFs	e	$\eta^{(3)}/e$
259	0.03601	1.71	199	0.09375	2.66	409	0.09375	0.03
905	0.03929	1.58	795	0.09376	2.66	817	0.09376	0.07
3455	0.03895	1.48	3207	0.09389	2.61	3255	0.09390	0.26
13673	0.03733	0.80	12869	0.08010	2.38	12979	0.08017	0.85
36791	0.03571	0.36	25880	0.04869	2.92	31670	0.04873	1.35

is more appropriate for guiding the adaptive refinement process and controlling errors for the entire QCEB model. Fig. 7(a) shows that the approximation errors of all four PDEs decrease uniformly as DOFs increase when the estimator is calculated by using the Poisson Eq. (3.6) (denoted by η_ϕ in the figure), i.e., the estimator η_ϕ is controlled by the parameter ϵ_1. The approximation error is defined as the ratio of the estimator to the approximate solution of each PDE in the maximum norm. When the other three estimators η_{r_n} (Eq. (3.7)), η_n (Eq. (3.9)), and η_{T_n} (Eq. (3.11)), were used, either the approximate potential (denoted by ϕ in the figure) or the quantum potential (r_n) or both did not converge as shown in Fig. 7(b)–(d). We thus conclude that the estimator η_ϕ (Poisson's Eq.) is more suitable to control the approximation errors of all PDEs in QCEB for the diode. Solution contours of the QCEB model using this estimator are shown in Fig. 8.

Table 5.3
Singular perturbation parameters (Diode).

ϵ_1^2	ϵ_2^2	ϵ_4^2	ϵ_6^2
$O(10^{-5})$	$O(10^{-8})$	$O(10^{-13}) \sim O(10^{3})$	$O(10^{-18}) \sim O(10^{1})$

Example 3. All seven PDEs in QCEB are needed to study an n-MOSFET device illustrated in Fig. 1, since holes are also major carriers in this kind of devices. The channel length is 28 nm and the doping has an elliptical 10^{19} cm^{-3} Gaussian profile in the source and drain regions and 10^{16} cm^{-3} in the p-substrate region. The junction depth is 18 nm, the lateral diffusion under gate is 6 nm, and the gate oxide thickness is 1.8 nm. The applied voltages are $V_{BS} = 0$, $V_{DS} = 0.85$, and $V_{GS} = 0.7$ V, where B, D, S, and G denote the bulk, drain, source, and gate contact, respectively. The numerical range of the singular parameters is given in Table 5.4,

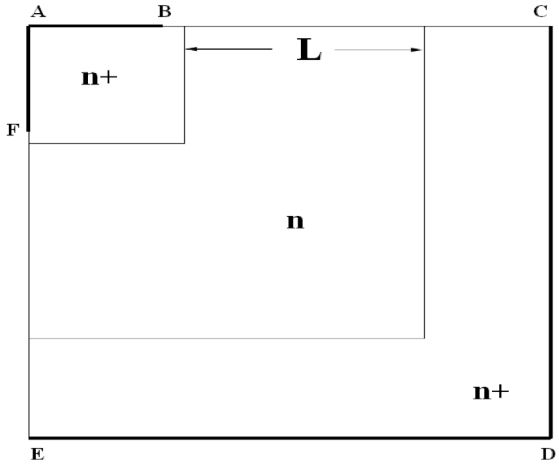

Fig. 6. An 80 nm × 80 nm $n^+ - n - n^+$ silicon diode for Example 2. Contacts are denoted by bold lines.

where we only provide the Planck (ϵ_2), DD (ϵ_4), and EB (ϵ_6) parameters for electrons as the corresponding parameters for holes are similar.

The range of DD and EB parameters is even more widely than that in Table 5.3, indicating that more energetic and sharp layering phenomena occur in MOSFET under these conditions. The estimator η_ϕ (associated with ϵ_1) is suitable for diode but not MOSFET since the approximation errors of the electron density n and temperature T_n are not reduced with increasing DOFs as shown in Fig. 9(a). The estimator η_{r_n} (with ϵ_2) obtained from the quantum equation (3.7) is even worse as shown in Fig. 9(b) since the quantum effect is only restricted to a very thin layer near the gate contact [5]. On the other hand, if we use the DD (η_n with ϵ_4) or

Table 5.4
Singular perturbation parameters (MOSFET).

ϵ_1^2	ϵ_2^2	ϵ_4^2	ϵ_6^2
$O(10^{-5})$	$O(10^{-8})$	$O(10^{-27}) \sim O(10^{3})$	$O(10^{-33}) \sim O(10^{1})$

EB (η_{T_n} with ϵ_6) estimator, the errors of ϕ and r_n are not reduced as shown in Fig. 9(c) and (d) since the DD and EB equations are more singular in the junction layers instead of the boundary layer [5].

The dimensionless formulation of QCEB is thus crucial for our methods in controlling errors because the resulting perturbation parameters in the seven dimensionless PDEs (3.6)–(3.12) can be used to calculate error estimators for these PDEs on equal footing. Tables 5.3 and 5.4 show that these parameters vary widely in numerical orders and Fig. 7(b)–(d) and Fig. 9(a)–(d) show that relative errors of a particular PDE may not be reduced by increasing DOFs if the mesh refinement is based on a single estimator of other PDE throughout without using the estimator of that particular PDE. And therefore the relative errors may not be uniformly convergent for all PDEs with respect to DOFs.

To deal with this nonuniform error reduction, the refinement criterion (4.12) is modified as

$$\eta_\gamma = \min\left\{\eta_{\gamma,\phi},\ \eta_{\gamma,r_n},\ \eta_{\gamma,n}\right\}, \tag{5.2}$$

where $\eta_{\gamma,\phi}$, η_{γ,r_n}, and $\eta_{\gamma,n}$ denote $\eta_\gamma^{(2)}$ in (4.12) corresponding to Eqs. (3.6), (3.7) and (3.9), respectively. Fig. 10 shows that the errors of seven PDEs are all uniformly reduced by using this hybrid estimator. A typical adaptive mesh by (5.2) for the QCEB results of MOSFET is shown in Fig. 11. The corresponding solution contours of the electrostatic potential ϕ, electron quantum potential ϕ_{q_n}, electron density n, and electron temperature T_n are shown in Fig. 12(a), (b), (c), and (d), respectively.

The adaptive mesh in Fig. 11 appears to be over-refined since the uniform error control of all seven PDEs is of interest

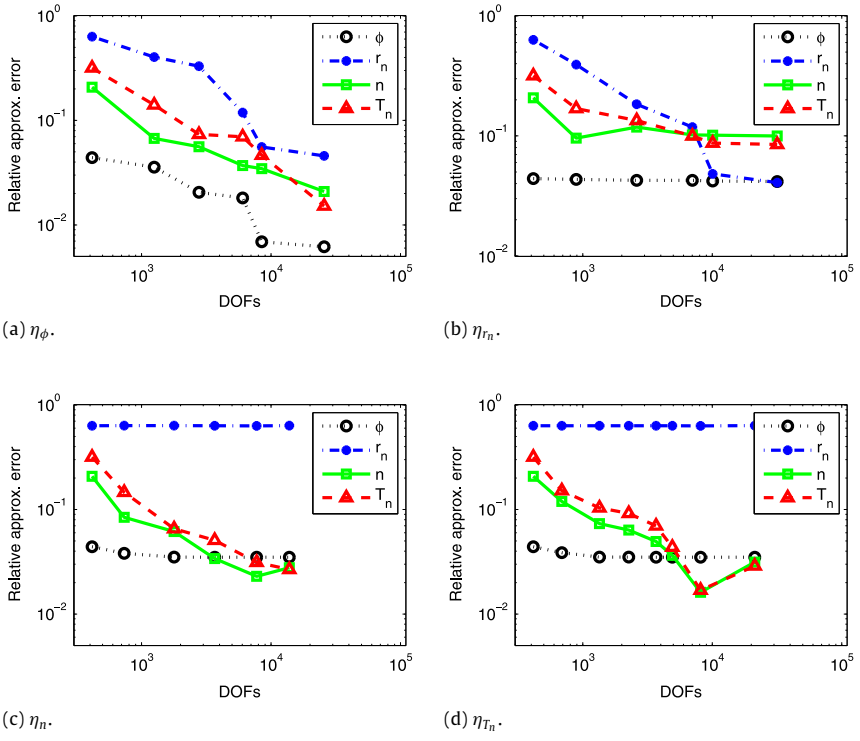

(a) η_ϕ. (b) η_{r_n}.

(c) η_n. (d) η_{T_n}.

Fig. 7. Uniform convergence of the QCET model for diode by the estimator η_ϕ (a) but nonuniform convergence by η_{r_n} (b), η_n (c), and η_{T_n} (d).

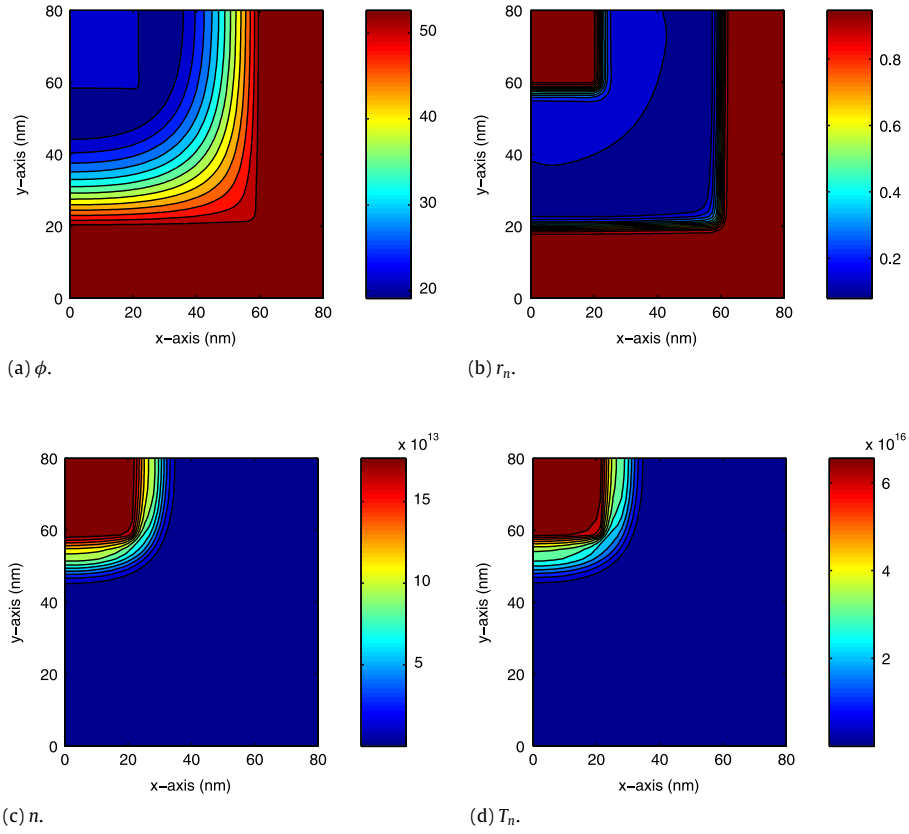

(a) ϕ. (b) r_n.

(c) n. (d) T_n.

Fig. 8. Solution contours of ϕ, r_n, $\widehat{n}$ and $\widehat{T_n}$ in Example 2 corresponding to Fig. 7(a).

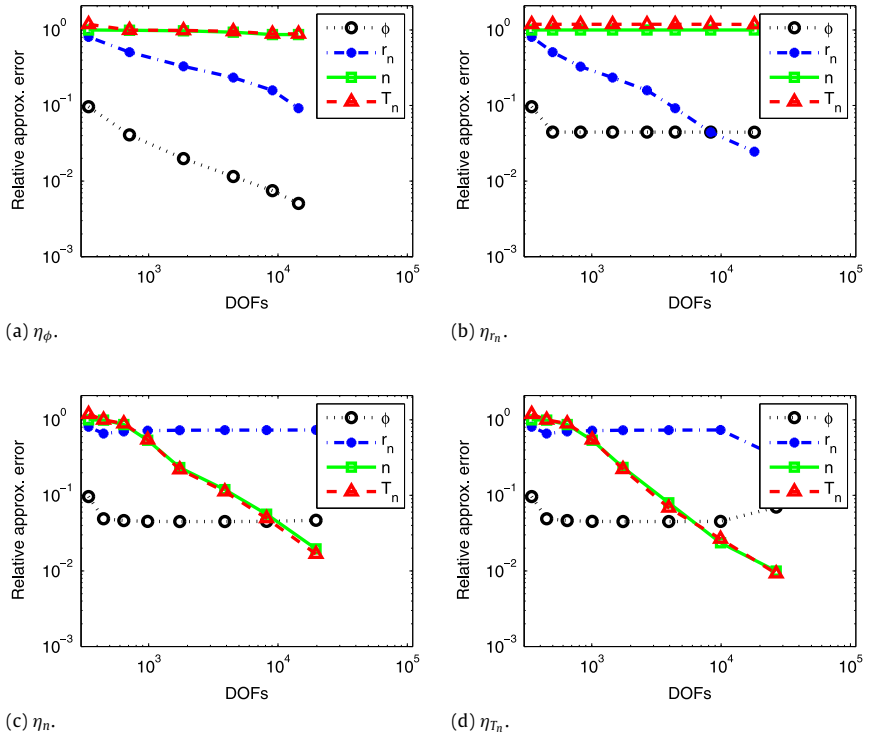

(a) η_ϕ. (b) η_{r_n}.

(c) η_n. (d) η_{T_n}.

Fig. 9. Nonuniform convergence of the QCET model for MOSFET in Example 3 by individual estimators η_ϕ, η_{r_n}, η_n, and η_{T_n}.

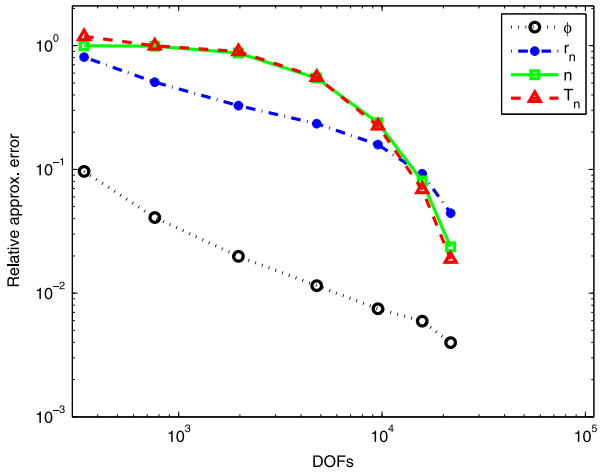

Fig. 10. Uniform convergence of the QCET model for MOSFET by the hybrid estimator (5.2).

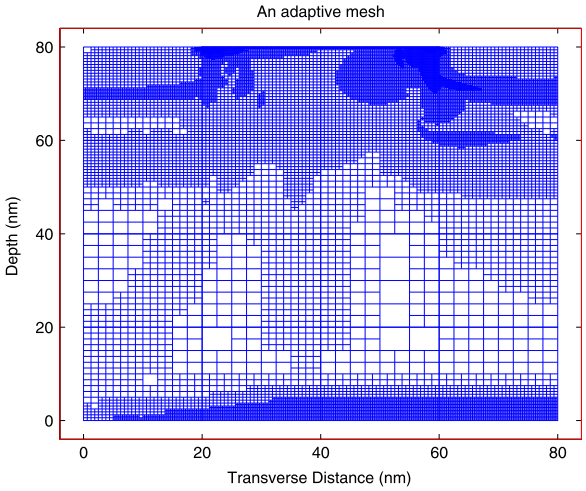

Fig. 11. An adaptive finite element mesh for MOSFET.

in this study as shown in Fig. 10. To predict I–V curves in realistic simulations, the present method should be compared with other methods in terms of mesh efficiency. We shall report our investigation elsewhere in this respect.

6. Conclusion

We have proposed a dimensionless form of a quantum energy transport (QCEB) model that consists of seven semilinear PDEs with the scaled Debye length, Planck constant, diffusivity, and thermal conductivity as singular perturbation parameters. The numerical range of these parameters has been shown to vary widely in different regions in two different semiconductor nanodevices—diode and MOSFET. We showed that the approximation errors of QCEB can be uniformly controlled by applying the second-order estimator of Kopteva [33] to different PDEs in QCEB during the adaptive mesh refinement process. Different parameters thus play different roles in refining different regions of the device in order to uniformly reduce all errors of QCEB in the adaptive process. The effectiveness of the estimator has been validated with a singularly PDE with exact solution. The error control method has been verified with extensive numerical results of the nanodevices.

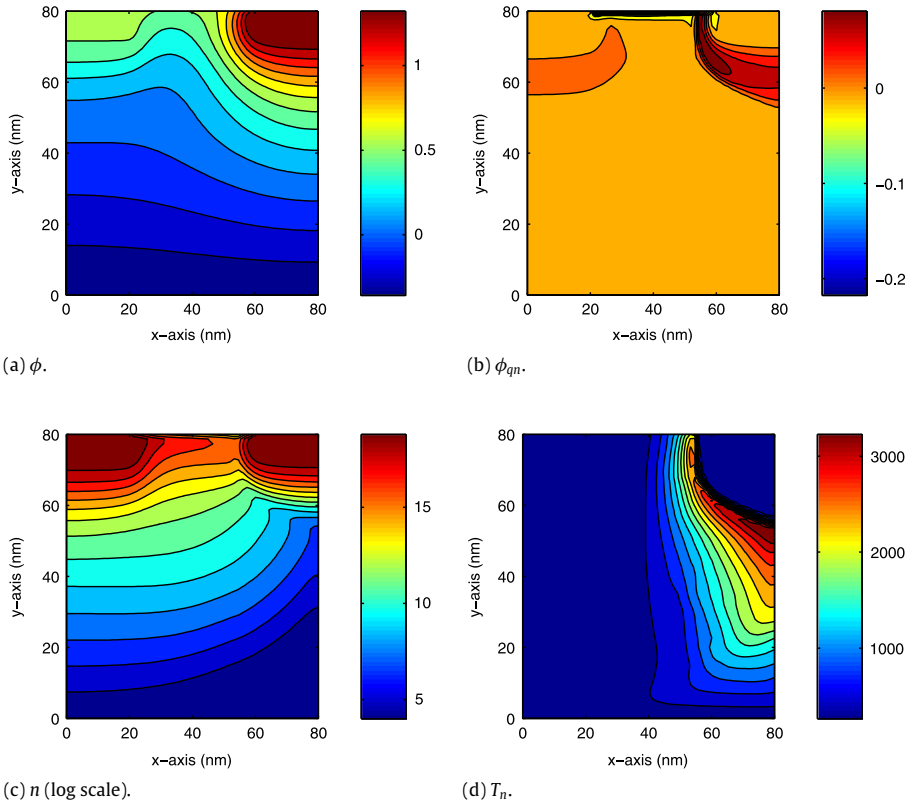

(a) ϕ. (b) ϕ_{qn}.

(c) n (log scale). (d) T_n.

Fig. 12. Solution contours of ϕ, r_n, $\widehat{n}$ and $\widehat{T_n}$ in Example 3.

References

[1] M.G. Ancona, H.F. Tiersten, Phys. Rev. B 35 (1987) 7959–7965.
[2] A. Asenov, A.R. Brown, J.H. Davies, S. Kaya, G. Slavcheva, IEEE Trans. Electron Devices 50 (2003) 1837–1852.
[3] N. Ben Abdallah, M. Mouis, C. Negulescu, J. Comput. Phys. 225 (2007) 74–99.
[4] B.A. Biegel, M.G. Ancona, C.S. Rafferty, Z. Yu, Efficient Multi-dimensional Simulation of Quantum Confinement Effects in Advanced MOS Devices, NAS Tech. Report NAS-04-008, 2004.
[5] R.-C. Chen, J.-L. Liu, J. Comput. Phys. 204 (2005) 131–156.
[6] V.D. Camiola, G. Mascali, V. Romano, J. Math. Comput. Model. 58 (2013) 321–343.
[7] C. de Falco, E. Gatti, A.L. Lacaita, R. Sacco, J. Comput. Phys. 204 (2005) 533–561.
[8] P. Degond, S. Gallego, F. Méhats, J. Comput. Phys. 221 (2007) 226–249.
[9] A. Jüngel, Math. Comput. Model. Dyn. Syst. 16 (2010) 1–22.
[10] A. Jüngel, A. El Ayyadi, SIAM J. Appl. Math. 66 (2005) 554–572.
[11] A. Jüngel, D. Matthes, J.P. Milišić, SIAM J. Appl. Math. 67 (2006) 46–68.
[12] A. Jüngel, S. Krause, P. Pietra, SIAM J. Appl. Math. 68 (2007) 171–198.
[13] M. Karner, A. Gehring, S. Holzer, M. Pourfath, M. Wagner, W. Goes, M. Vasicek, O. Baumgartner, C. Kernstock, K. Schnass, G. Zeiler, T. Grasser, H. Kosina, S. Selberherr, J. Comput. Electron. 6 (2007) 179–182.
[14] A. Martinez, J.R. Barker, A. Asenov, A. Svizhenko, M. Bescond, A. Anantram, IEEE SISPAD (2006) 353–356.
[15] S. Roy, A. Asenov, Science 309 (2005) 388–390.
[16] S. Sho, S. Odanaka, J. Comput. Phys. 235 (2013) 486–496.
[17] D. Vasileska, S.S. Ahmed, IEEE Trans. Electron Devices 52 (2005) 227–236.
[18] C. de Falco, J.W. Jerome, R. Sacco, J. Comput. Phys. 228 (2009) 1770–1789.
[19] A. Dutta, S. Sirohi, T. Ethirajan, H. Agarwal, Y.S. Chauhan, R.Q. Williams, 13th Int. Conf. on Embedded Systems, 2014.
[20] Y.-B. Liao, M.-H. Chiang, N. Damrongplasit, W.-C. Hsu, T.-J.K. Liu, IEEE Trans. Electron Devices 61 (2014) 2371–2377.
[21] P. Degond, C. Ringhofer, J. Stat. Phys. 112 (2003) 587–628.
[22] S. Odanaka, IEEE Trans. Comput.-Aided Des. Integr. Circuits Syst. 23 (2004) 837–842.
[23] D. Bohm, Phys. Rev. 85 (1952) 166–193.
[24] E. Pop, S. Sinha, K.E. Goodson, Proc. IEEE 94 (2006) 1587–1601.
[25] D. Vasileska, K. Raleva, S.M. Goodnick, J. Comput. Electron. 7 (2008) 179–182.
[26] C.L. Gardner, SIAM J. Appl. Math. 54 (1994) 409–427.
[27] U. Ascher, P. Markowich, C. Schmeiser, H. Steinruck, R. Weiss, SIAM J. Appl. Math. 49 (1989) 165–185.
[28] F. Brezzi, L.D. Marini, P. Pietra, SIAM J. Numer. Anal. 26 (1989) 1342–1355.
[29] R.-C. Chen, J.-L. Liu, J. Comput. Appl. Math. 159 (2003) 341–364.
[30] R.-C. Chen, J.-L. Liu, J. Comput. Phys. 227 (2008) 6266–6240.
[31] R.-C. Chen, J.-L. Liu, J. Comput. Phys. 189 (2003) 579–606.
[32] Y. Li, J.-L. Liu, S.M. Sze, T.-S. Chao, Comput. Phys. Comm. 142 (2001) 285–289.
[33] N. Kopteva, SIAM J. Numer. Anal. 46 (2008) 1602–1618.
[34] N. Kopteva, E. O'Riordan, Int. J. Numer. Anal. Model. 7 (2010) 393–415.
[35] P.F. Antonietti, L.B. da Veiga, C. Lovadina, M. Verani, SIAM J. Numer. Anal. 51 (2013) 654–675.
[36] N.M. Chadha, N. Kopteva, IMA J. Numer. Anal. 31 (2011) 188–211.
[37] Z. Chen, Y. Xiao, L. Zhang, J. Comput. Phys. 228 (2009) 5000–5019.
[38] X. Zhao, S. Mao, Z.-C. Shi, J. Comput. Math. 28 (2010) 621–644.
[39] M. Ainsworth, J.T. Oden, A Posteriori Error Estimation in Finite Element Analysis, vol. 37, John Wiley & Sons, 2011.
[40] I. Babuška, T. Strouboulis, The Finite Element Method and Its Reliability, Oxford Science Publications, 2001.
[41] T. Gräsch, K.-J. Bathe, Comput. Struct. 83 (2005) 235–265.
[42] J.-L. Liu, SIAM J. Sci. Comput. (1996) 1249–1268.
[43] R. Verfürth, A Review of A Posteriori Error Estimation and Adaptive Mesh Refinement Techniques, John Wiley & Sons, 1996.
[44] V. John, Comput. Methods Appl. Mech. Engrg. 190 (2000) 757–781.
[45] A. Demlow, N. Kopteva, Maximum-norm a posteriori error estimates for singularly perturbed elliptic reaction–diffusion problems, Preprint, 2014.
[46] M. Stynes, Acta Numer. 14 (2005) 445–508.
[47] J.-L. Liu, I.-J. Lin, M.-Z. Shih, R.-C. Chen, M.-C. Hsieh, Appl. Numer. Math. 21 (1996) 439–467.
[48] O.C. Zienkiewicz, A.W. Craig, in: I. Babuska, et al. (Eds.), Accuracy Estimates and Adaptive Refinements in Finite Element Computations, Wiley, New York, 1986, pp. 25–59.